

Characterizing spin transport: detection of spin accumulation via magnetic stray field

Matthias Pernpeintner,^{1,2,3} Akashdeep Kamra,^{4,1} Sebastian T.B. Goennenwein,^{5,6,1,2,3} and Hans Huebl^{1,2,3,*}

¹*Walther-Meißner-Institut, Bayerische Akademie der Wissenschaften, Garching, Germany*

²*Nanosystems Initiative Munich, München, Germany*

³*Physik-Department, Technische Universität München, Garching, Germany*

⁴*Department of Physics, University of Konstanz, Konstanz, Germany*

⁵*Institut für Festkörperphysik, Technische Universität Dresden, Dresden, Germany*

⁶*Center for Transport and Devices of Emergent Materials, Technische Universität Dresden, Dresden, Germany*

Spin transport in electric conductors is largely determined by two material parameters - spin diffusion length and spin Hall angle. In metals, these are typically determined indirectly by probing magnetoresistance in magnet/metal heterostructures, assuming knowledge of the interfacial properties. We suggest profiling the charge current induced spin Hall spin accumulation in metals, via detection of the magnetic stray field generated by the associated static magnetization, as a direct means of determining spin transport parameters. We evaluate the spatial profile of the stray field as well as the Oersted field generated by the charge current. We thus demonstrate that such a charge current induced spin accumulation is well within the detection limit of contemporary technology. Measuring the stray fields may enable direct access to spin-related properties of metals paving the way for a better and consistent understanding of spin transport therein.

I. INTRODUCTION

The field of spintronics investigates the interplay between the spin (magnetic) and charge degrees of freedom in a solid-state system^{1,2}. Initial experimental techniques have focused on the electronic or optical detection of the magnetization, where the latter is controlled or initialized via an external magnetic field. It has subsequently been realized that the magnetization direction can also be manipulated via spin-polarized charge currents utilizing the phenomenon of spin-transfer torques (STT)³⁻⁵. The physics underlying STT may be understood with reference to a simple model in which the magnetization results from the localized d-electrons while the mobile s-electrons mediate transport. Due to an exchange coupling between the s and d electrons, the mobile s-electrons experience a torque exerted by the magnetization. Reciprocally, the magnetization experiences an equal and opposite torque. This technique has successfully been employed for magnetization switching and domain wall motion, and forms the basis for a number of devices such as racetrack⁶ and STT-magnetoresistive random access memories⁷.

While the mechanism for spin-polarization of current relies on the conductor magnetization in the above mentioned devices, pure spin currents have also been generated and detected in non-magnetic materials, with spin-orbit interaction enabling interconversion between charge and spin currents⁸⁻¹⁰. Although there are a number of microscopic mechanisms contributing to this interconversion¹¹, a simple picture is provided by asymmetric scattering from impurities. An electron experiences, due to spin-orbit interaction, a spin-dependent impurity potential and scattering probability in the transverse direction (see Fig. 1). Thus, a charge flow leads to a spin current in the transverse direction and vice-versa. This phenomenon has been termed spin Hall effect (SHE) and the conversion efficiency is quantified by the so-called spin

Hall angle (θ). Since the spin current cannot escape the material, a spin accumulation builds up close to the conductor edges so that the diffusive backflow compensates the SHE current at the edge. This spin accumulation decays exponentially over a distance, called spin diffusion length (λ), from the interface and is well described within a diffusive transport theory¹².

In heterostructures comprising a magnet (F) and a non-magnetic metal (N)¹³, the transport and magnetization electrons may be spatially separated. One mechanism for STT in these systems is via the SHE mediated accumulation of electron spins at the interface, when a charge current is driven in N. In addition to altering or moving the magnetic textures, STT also enables injection of pure spin currents into the magnetic material. This interplay between electronic and magnonic spin currents¹⁴ is exemplified by phenomena like spin pumping^{15,16}, electrical spin injection¹⁷, spin Seebeck effect¹⁸⁻²⁰, and spin Hall magnetoresistance (SMR)²¹⁻²⁴.

Different methods for spin accumulation detection are necessary in different materials. In semiconductors, direct spatially resolved optical detection has been achieved via Kerr rotation measurements^{25,26} and recently, Stamm et al. reported (non-spatially resolved) detection of the spin accumulation in metal thin films²⁷. The latter turns out to be challenging in metals due to their small electromagnetic field penetration depths and the resulting Kerr angles of the order of 10×10^{-9} rad. Typical techniques employed in metals rely therefore on examining an effect of the spin accumulation and constitute an indirect measurement. For example, the N thickness dependence of SMR in an F|N heterostructure allows inferring the spin Hall angle, but the approach relies on accurate knowledge about the interface and the interplay between the material systems^{28,29}. These interfacial properties are not easily determined and vary in a wide range¹⁴.

Here we suggest to detect SHE mediated spin accu-

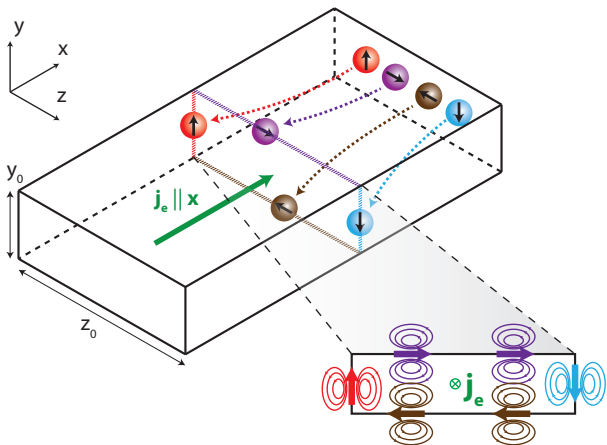


FIG. 1. Schematic illustration of SHE mediated spin separation and accumulation in a metallic strip. The conductor is assumed long with width z_0 and thickness y_0 . A charge current density j_e flows along the x -direction. Due to spin Hall effect (SHE), the conduction electrons are scattered in different directions depending on their spin polarization: Up-spins (red; polarized along \hat{y}), e.g., are deflected in the $-z$ -direction, while down-spins (blue; polarized along \hat{y}) are deflected in the $+z$ -direction. This results in an accumulation of spin-polarized electrons at the surfaces of the strip. The resulting magnetization close to the edges and the magnetic fields induced by these moments are illustrated, respectively, by colored arrows and black lines. The field lines indicate the net magnetic stray field around the strip, i.e. the sum of the stray and Oersted fields.

mulation, and thus characterize spin transport parameters, in a metallic strip by measuring the magnetic ‘stray’ field resulting from the non-equilibrium magnetization associated with the spin-polarized electrons. While the net magnetic moment in the system vanishes, a finite magnetization is generated near the boundaries of the

metal. We evaluate the ensuing stray field analytically within a simplified model as well as numerically, and find that the field is well within the detection range of the state-of-the-art sensing techniques such as NV centers^{30–32}, magnetic force microscopy^{33,34}, scanning SQUID magnetometers^{35,36}, or muon spin resonance³⁷. We further show that the magnetic stray field of spin accumulation may exceed and can be disentangled from the Oersted field arising due to the current flow, that generates the spin accumulation via SHE, using their distinct spatial profiles. The proposed method thus enables a direct access to important spin transport properties - spin diffusion length λ and the spin-Hall angle θ in metals - while circumventing the difficulties associated with F|N interfaces.

The paper is organized as follows: In Section II, we derive the spin accumulation profile in the metallic strip (Fig. 1) and obtain an analytic expression for the magnetic stray field at large (compared to λ) distances from the surface. Section III discusses the spatial magnetic field distribution evaluated using the approximate analytic expression as well as numerically. In Section IV we evaluate the Oersted field distribution generated by the charge current in the strip. We discuss the field distribution for a multilayer system in Sec. V and demonstrate that the Oersted field can be reduced significantly by allowing a counterflow of current in an adjacent layer. We conclude with discussion of experimental issues and a short summary of our results in Section VI.

II. SPIN ACCUMULATION AND MAGNETIC STRAY FIELD

We consider a long metallic strip with width z_0 and thickness y_0 which supports a charge current density of j_e driven by an electric field $E_0\hat{x}$ along its length (Fig. 1). The general current response in a non-magnetic conductor including SHE reads¹²:

$$\begin{pmatrix} \mathbf{j}_e \\ \mathbf{j}_{sx} \\ \mathbf{j}_{sy} \\ \mathbf{j}_{sz} \end{pmatrix} = \sigma_N \begin{pmatrix} 1 & \theta\hat{x}\times & \theta\hat{y}\times & \theta\hat{z}\times \\ \theta\hat{x}\times & 1 & 0 & 0 \\ \theta\hat{y}\times & 0 & 1 & 0 \\ \theta\hat{z}\times & 0 & 0 & 1 \end{pmatrix} \begin{pmatrix} \mathbf{E} \\ -\nabla\mu_{sx}/2e \\ -\nabla\mu_{sy}/2e \\ -\nabla\mu_{sz}/2e \end{pmatrix}, \quad (1)$$

where σ_N is the conductivity, $e(> 0)$ is the electronic charge, θ is the spin Hall angle, \mathbf{j}_e is the charge current density, \mathbf{E} is the applied electric field, and \mathbf{j}_{si} is the spin current density polarized in the i -direction ($i = x, y, z$). μ_{si} is the corresponding spin chemical potential, which obeys the diffusion equation:^{38–40}

$$\nabla^2\mu_{si} = \frac{\mu_{si}}{\lambda^2}, \quad (2)$$

with the spin diffusion length λ . The boundary conditions for (2) are vanishing spin current flow normal to all interfaces, which in the chosen coordinate system read:

$$j_{si}^y(y = \pm y_0/2) = 0 \quad \text{and} \quad j_{si}^z(z = \pm z_0/2) = 0. \quad (3)$$

Here the superscript denotes the spatial direction of spin current flow while the subscript represents the spin polarization direction. The diffusion equation (2) with the

boundary conditions [Eq. (3)] admits the solution⁴¹:

$$\mu_{sy}(\mathbf{r}) = -2e\theta\lambda E_0 \frac{\sinh(z/\lambda)}{\cosh(z_0/(2\lambda))}, \quad (4)$$

$$\mu_{sz}(\mathbf{r}) = 2e\theta\lambda E_0 \frac{\sinh(y/\lambda)}{\cosh(y_0/(2\lambda))}, \quad (5)$$

where \mathbf{r} is the position vector. As detailed in Appendix A, the spin accumulation density is related to the spin chemical potential by⁴⁰

$$n_{si} = \frac{\sigma_N}{2e^2 D} \mu_{si}, \quad (6)$$

where $D = \lambda^2/\tau$ denotes the electron diffusion constant^{12,42} and τ is the spin-flip time. The n_{si} are defined as $n_{si} = n_\uparrow - n_\downarrow$, where the subscript arrows \uparrow, \downarrow denote the up- and down-polarized spins for the respective quantization axes.

The spin accumulation is thus spatially localized to a region within $\sim \lambda$ from the surfaces. While the exact evaluation of the magnetic field arising from this charge-current induced magnetization requires numerics, analytical expressions can be obtained in the limit of $\lambda \ll r_p$, where \mathbf{r}_p is the position vector of the point at which the magnetic field is measured. We refer to this as the ‘far-field limit’. Relegating the details to Appendix B, the magnetic field distribution $\mathbf{B}(\mathbf{r}_p)$ in this limit is evaluated as:

$$\mathbf{B}(\mathbf{r}_p) = \frac{\mu_0 \gamma \hbar j_e \theta \tau}{8\pi e} \left(\frac{1}{\cosh\left(\frac{y_0}{2\lambda}\right)} - \frac{1}{\cosh\left(\frac{z_0}{2\lambda}\right)} \right) \mathbf{F}(y_0, z_0; \mathbf{r}_p), \quad (7)$$

$$\mathbf{F}(y_0, z_0; \mathbf{r}_p) = \sum_{\sigma_1, \sigma_2 = \pm 1} \frac{2(y_p - \sigma_1 y_0/2)}{(y_p - \sigma_1 y_0/2)^2 + (z_p - \sigma_2 z_0/2)^2} \hat{\mathbf{y}} + \frac{2(z_p - \sigma_2 z_0/2)}{(y_p - \sigma_1 y_0/2)^2 + (z_p - \sigma_2 z_0/2)^2} \hat{\mathbf{z}}, \quad (8)$$

where μ_0 is the permeability of free space and γ is the gyromagnetic ratio in the metal. From the expression above, we note that a high aspect ratio leads to larger stray field. Thus it is desirable to have the metal in the shape of a film.

III. MAGNETIC STRAY FIELD: SPATIAL PROFILE

We next compute the spatial distribution of the stray field originating from spin accumulation for the example of a platinum (Pt) conductor. The material parameters employed²⁸ are spin Hall angle $\theta = 0.08$, electric conductivity $\sigma_N = 9.52 \times 10^6$ A/Vm, spin diffusion length $\lambda = 4$ nm, spin flip time $\tau = 60$ ps⁴³ and $\gamma\hbar = \mu_B = 9.27 \times 10^{-24}$ J/T. For the geometric dimensions of the Pt strip we choose $y_0 = 2$ nm and $z_0 = 30$ nm and we assume a current density $j_e = 1 \times 10^{10}$ A/m².

With these material parameters, we calculate the spin accumulation at the surfaces $|n_{sy}(z = \pm z_0/2)| = 7.8 \times 10^{25}$ m⁻³ and $|n_{sz}(y = \pm y_0/2)| = 1.9 \times 10^{25}$ m⁻³. This corresponds to a net spin polarisation of about 0.1 percent present at the interface⁴⁴. As evident from Eqs. (4) and (5), the spin polarisation decays exponentially with decay length λ into the body of the metal, as shown in Fig. 2.

The corresponding spatial distribution of the magnetic stray field calculated numerically (see Appendix) is plotted in Fig. 3a. Here, the gray transparent box indicates the conductor cross-section. The stray field diverges at

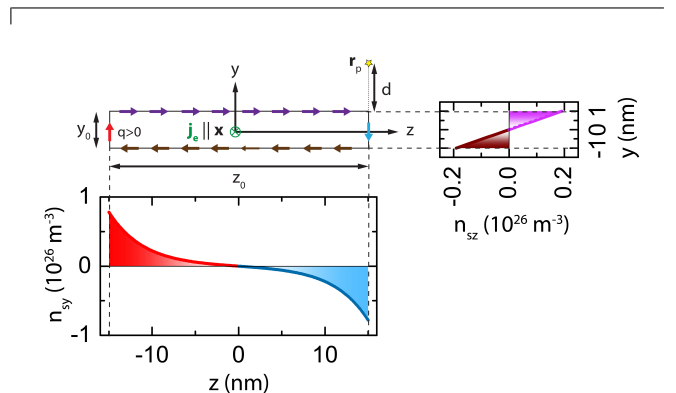


FIG. 2. Schematic illustration of the spin accumulation in the platinum strip, shown together with the calculated spin accumulation as a function of y resp. z .

the edges of the strip, exceeding 20 μ T within a radius of about $d = 5$ nm (Fig. 3a). The stray field calculated using Eq. (7) matches the numerical solution very well at large distances (Fig. 3c). Near the conducting strip, however, the approximation (7) leads to significant errors. In the far-field limit, the stray field decays $\sim 1/r_p^3$.

IV. OERSTED FIELD: SPATIAL PROFILE

Relegating the evaluation details to Appendix C, we discuss the magnetic field distribution of the Oersted field $\mathbf{B}_{\text{Oer}}(\mathbf{r}_p)$ created by the charge current flow in the conductor. Figure 4 shows the spatial distribution of the

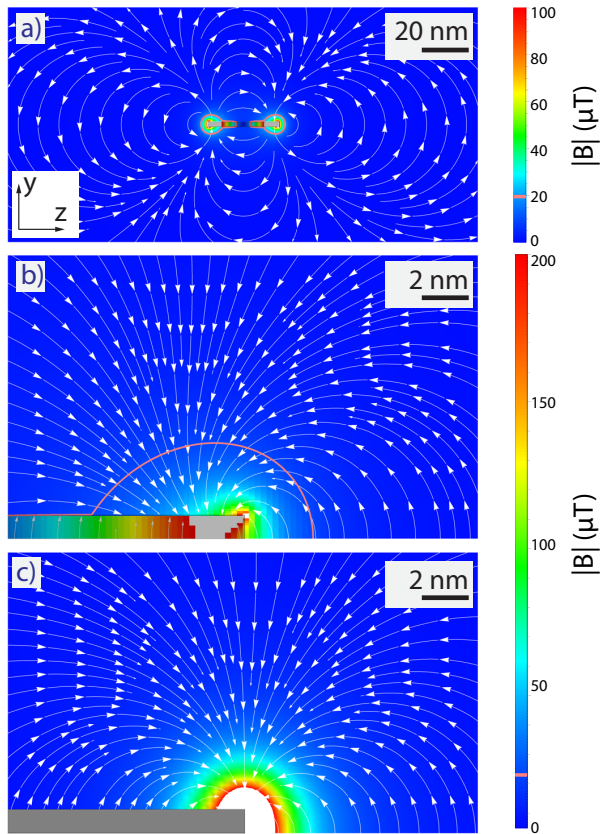


FIG. 3. Magnetic stray field profile $\mathbf{B}(\mathbf{r}_p)$ of spin accumulation in the conducting strip evaluated (a) and (b) numerically as well as (c) analytically using Eq. (7). The white arrows indicate the magnetic field direction, the color encodes its magnitude, where white regions indicate fields above $200 \mu\text{T}$. The transparent (solid) gray rectangle depicts the cross-section of the metal strip for the numerical (analytical) evaluation. The pink solid line represents the $20 \mu\text{T}$ contour line. Panels (b) and (c) show a zoom-in around the top-right edge of the strip to compare the numerical and analytical model.

Oersted field around the conductor. It has its maximum of about $16 \mu\text{T}$ at the left and right edge of the strip. In the far-field limit, the Oersted field decays proportional to $1/r_p$ as expected for the far-field. Thus, at large distances the Oersted field dominates the stray field. This is also illustrated in Fig. 5, where the ratio $|\mathbf{B}|/|\mathbf{B}_{\text{Oer}}|$ is plotted as a function of the sensor position \mathbf{r}_p including white solid line indicating $|\mathbf{B}|/|\mathbf{B}_{\text{Oer}}| = 1$. Nevertheless, the spatial dependence of the Oersted field significantly differs from that of the magnetic stray field of spin accumulation. Thus, using a spatially resolved magnetic field sensing technique should allow to disentangle the SHE induced stray field from the Oersted field.

V. TRILAYER GEOMETRY

In order to suppress the contribution of the Oersted field to the total magnetic field, we suggest a trilayer

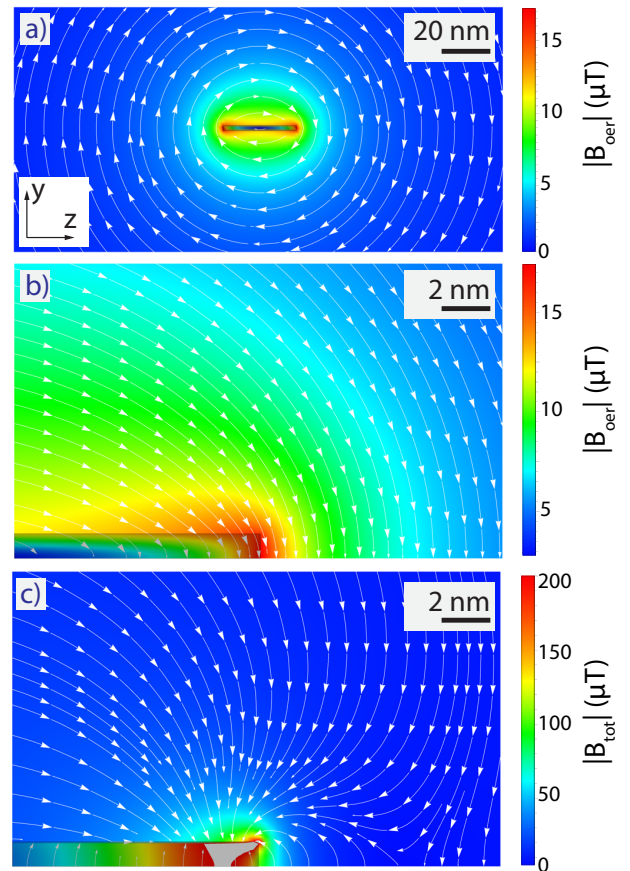


FIG. 4. Oersted field $\mathbf{B}_{\text{Oer}}(\mathbf{r}_p)$ as a function of the sensor position \mathbf{r}_p . Panel (b) depicts a zoom-in of the upper right edge and panel (c) shows the total magnetic field $|\mathbf{B}_{\text{tot}}| = |\mathbf{B} + \mathbf{B}_{\text{Oer}}|$.

sample geometry where the strip consists of two conducting layers with a thin insulating layer (thickness d_{ins}) in between. We consider the upper layer (thickness y_0) to have a large spin Hall angle θ , while the spin Hall angle of the lower conducting layer (thickness y'_0) vanishes. In the following we discuss the situation, where current flows through both conducting layers with equal magnitude but opposite signs. In the near field, the trilayer geometry reduces the Oersted field contribution. As we assume the spin Hall angle in the bottom conducting layer to be zero, the stray field of the top layer is not affected by the bottom layer. As a consequence, the ratio B/B_{Oer} can be increased significantly.

For a quantitative analysis, we calculate both the stray field and the Oersted field around the trilayer geometry as a function of the sensor position \mathbf{r}_p . We here set $y_0 = y'_0 = 2 \text{ nm}$, $d_{\text{ins}} = 2 \text{ nm}$ and $z_0 = 30 \text{ nm}$ ⁴⁵ and leave the material parameters unchanged. Figure 6 shows the calculated Oersted field for this trilayer geometry. Compared to the above discussed single-layer geometry (see Fig. 4), we observe a significant suppression of the Oersted field. The ratio $B/B_{\text{Oer,TL}}$, plotted in Fig. 7a, shows

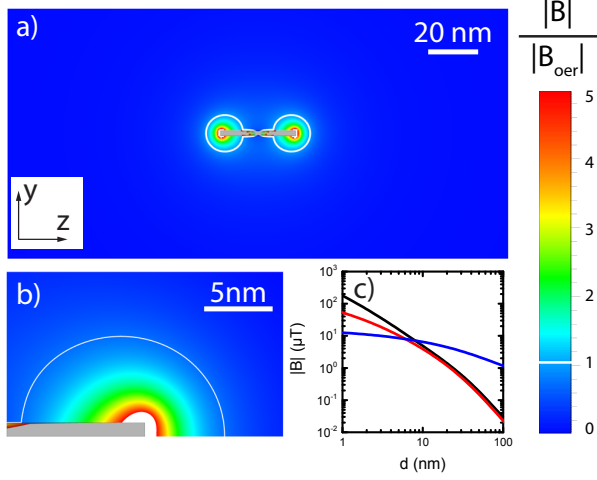


FIG. 5. **a.** $|\mathbf{B}|/|\mathbf{B}_{\text{oeer}}|$ as a function of y_p and z_p . The white solid line represents the $|\mathbf{B}|/|\mathbf{B}_{\text{oeer}}| = 1$ contour line indicating that the spin accumulation induced stray field exceeds the Oersted field significantly. Areas, where $|\mathbf{B}|/|\mathbf{B}_{\text{oeer}}|$ exceeds 5 are displayed in white. The gray (semi-transparent) rectangle depicts the cross-section of the metal strip. **b.** Close-up of the edge region of the strip. **c.** $|\mathbf{B}|$ and $|\mathbf{B}_{\text{oeer}}|$ as a function of d for the sensor position depicted in Fig. 2. The solid red (black) line corresponds to the full numerical (analytical, i.e. (7)) computation of $|\mathbf{B}|$, while the blue line depicts $|\mathbf{B}_{\text{oeer}}|$. We find $|\mathbf{B}|/|\mathbf{B}_{\text{oeer}}| > 1$ for $d \lesssim 6$ nm.

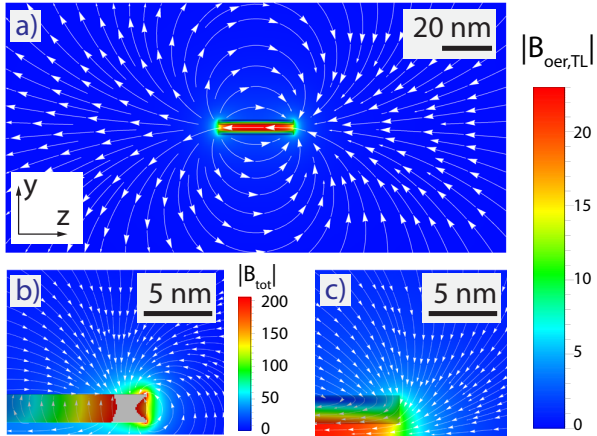


FIG. 6. **a.** Oersted field $\mathbf{B}_{\text{oeer,TL}}$ as a function of y_p and z_p for the proposed trilayer sample. The semi-transparent rectangles depict the cross-sections of the two metal strips. **b.** Total magnetic field $\mathbf{B}_{\text{tot}} = \mathbf{B} + \mathbf{B}_{\text{oeer,TL}}$ close to the edge of the upper conductive strip. **c.** Oersted field of the same region for comparison.

maxima around the edges of the top strip where the stray field clearly dominates the Oersted field. In particular, we find that the ratio of stray field and Oersted field, B/B_{oeer} , is 5.5 at $d = 5$ nm and 3.4 at $d = 10$ nm. Thus the contribution of the spin accumulation to the total magnetic field around the conductor is easily detectable

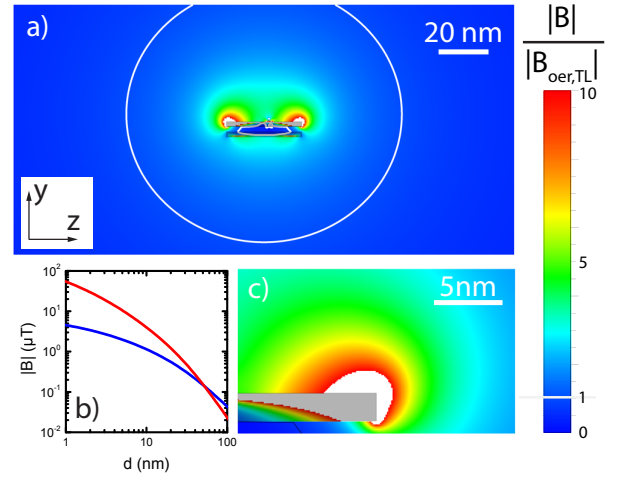


FIG. 7. **a.** and **c.** Field ratio $|\mathbf{B}|/|\mathbf{B}_{\text{oeer,TL}}|$ as a function of y_p and z_p for the proposed trilayer sample. The white solid line represents the $|\mathbf{B}|/|\mathbf{B}_{\text{oeer,TL}}| = 1$ contour line. Areas, where $|\mathbf{B}|/|\mathbf{B}_{\text{oeer,TL}}| > 10$ are also shaded in white. The gray (semi-transparent) rectangle depicts the cross-section of the metal strip. **b.** $|\mathbf{B}|$, $|\mathbf{B}_{\text{oeer,TL}}|$ and $|\mathbf{B}_{\text{oeer}}|$ as a function of d for the sensor position depicted in Fig. 2. **c.** $|\mathbf{B}|$ and $|\mathbf{B}_{\text{oeer,TL}}|$ as a function of d for the sensor position depicted in Fig. 2. The solid red line corresponds to the full numerical computation of $|\mathbf{B}|$, while the blue line depicts $|\mathbf{B}_{\text{oeer}}|$ of the trilayer configuration. We find $|\mathbf{B}|/|\mathbf{B}_{\text{oeer}}| > 1$ for $d \lesssim 50$ nm.

and quantifiable in the presented geometry.

Table V lists the y -components of magnetic field B_y and magnetic field gradient $\partial B_y/\partial y$ for a sample-sensor distance of $d = 5$ nm and $d = 20$ nm (cf. Fig 2). The d -dependence of stray and Oersted fields is depicted in Fig. 7b. We find that the Oersted farfield around the proposed trilayer sample decays proportional to $1/r_p^2$, compared to $1/r_p$ for the Oersted field of a single conducting layer. Besides, fig. 7b shows the $1/r_p^3$ -dependence of the stray field. As a consequence, in trilayer geometry, up to $d = 100$ nm away from the edges, the magnetic stray field exceeds the Oersted field of the two conducting layers.

VI. DISCUSSION AND SUMMARY

We consider magnetic force microscopy (MFM) as a potential candidate for the measurement of the stray field

TABLE I. y -components of magnetic field B_y and magnetic field gradient $\partial B_y/\partial y$ for a sample-sensor distance of $d = 10$ nm and $d = 5$ nm (trilayer sample geometry).

| | | Stray field | | Oersted field | |
|-------------------|---------------------------|----------------------|----------------------|---------------|--|
| $d = 10\text{nm}$ | B_y | $-3.6 \mu\text{T}$ | $-1.0 \mu\text{T}$ | | |
| | $\partial B_y/\partial y$ | 460 T/m | 100 T/m | | |
| $d = 5\text{nm}$ | B_y | $-8.8 \mu\text{T/m}$ | $-1.9 \mu\text{T/m}$ | | |
| | $\partial B_y/\partial y$ | 1560 T/m | 282 T/m | | |

profile^{46,47} and estimate the sensitivity required. The force acting on a MFM tip is $\mathbf{F} = (\mathbf{m} \cdot \nabla)\mathbf{B}$, where $\mathbf{m} = (0, m, 0)$, $m \approx 1 \times 10^{-13} \text{ emu} = 1 \times 10^{-16} \text{ Am}^2$ is typical magnetic moment of a MFM tip⁴⁸. Using $\partial B_y / \partial y$ from Tab. V, we expect a force in y -direction, $|F_y|$, of 46 fN (for $d = 10 \text{ nm}$) or 156 fN ($d = 5 \text{ nm}$), respectively. The state-of-the-art sensitivity concerning force measurements using MFM is about 10 fN at room temperature⁴⁹. Besides, Mamin et al.⁵⁰ have reported the detection of aN forces with MFM operated at 100 mK. Using MFM in frequency-modulated detection mode, force gradient sensitivities down to 0.14 $\mu\text{N/m}$ have been reported⁵¹. This is well below the expected stray field force gradients $\partial F_y / \partial y = 7.8 \mu\text{N/m}$ ($d = 20 \text{ nm}$) and $\partial F_y / \partial y = 45 \mu\text{N/m}$ ($d = 5 \text{ nm}$).

In summary, we have discussed a direct method to detect spin accumulation in a non-magnetic metal strip. The proposed approach is based on the measurement of the magnetic stray field arising from the electron spin accumulation close to the surfaces of the metal strip. To this end, we have derived an analytical expression for the spin accumulation and the corresponding magnetic stray field around a non-magnetic, metallic strip with rectangular cross-section. Based on this, we proposed a sample geometry for a future experiment and calculated the spatial distribution of the magnetic stray field. We showed that the stray field is large enough for detection using the state-of-the-art sensing techniques. Besides, we compared the stray field to the Oersted field around the non-magnetic conductor and found that for the proposed trilayer sample geometry, the Oersted field is dominated by the stray field near the edges of the conducting strip. Such a direct detection of spin accumulation should enable a reliable measurement of spin transport properties, such as spin diffusion length and spin Hall angle, in metals thereby circumventing interfacial complexities.

ACKNOWLEDGMENTS

We acknowledge funding from DFG via Priority program 1538 Spin-Caloric Transport (Project GO 944/4) and SPP1601 (HU 1896/2). AK is funded by A. v. Humboldt foundation.

Appendix A: Relation between spin chemical potential and spin density

In order to derive the relation between spin chemical potential and spin density in a non-magnetic conductor, we consider a degenerate non-magnetic gas and obtain relation between spin accumulation and spin density using a two spin channel model. The discussion herein borrows heavily from Ref. 40. For a Fermion gas, we have:

$$n = \int g(E) f(E - \mu) dE,$$

where n denotes the density of electrons, $g(E)$ is the density of states per unit volume, μ is the chemical potential, and $f(x) = 1/(\exp(x/k_b T) + 1)$ is the Fermi function. For a two spin model, the above equation becomes:

$$n_{\uparrow, \downarrow} = \int g_{\uparrow, \downarrow}(E) f(E - \mu_{\uparrow, \downarrow}) dE.$$

Here, the subscript arrows \uparrow, \downarrow denote two opposite spin direction (up and down, resp. left and right). For a non-magnetic conductor, $g_{\uparrow}(E) = g_{\downarrow}(E) = g(E)/2$ with $g(E)$ as the total density of states per unit volume. In addition, we define the following notation:

$$n = n_{\uparrow} + n_{\downarrow}, \quad (\text{A1})$$

$$s = n_{\uparrow} - n_{\downarrow}, \quad (\text{A2})$$

$$\mu = \frac{\mu_{\uparrow} + \mu_{\downarrow}}{2}, \quad (\text{A3})$$

$$\mu_s = \frac{\mu_{\uparrow} - \mu_{\downarrow}}{2}. \quad (\text{A4})$$

Further we assume, $\mu_s \ll \mu$ for a linear response theory. Having defined the above notation we proceed to express s in terms of spin chemical potential μ_s .

$$\begin{aligned} s &= n_{\uparrow} - n_{\downarrow}, \\ &= \frac{1}{2} \int g(E) (f(E - \mu_{\uparrow}) - f(E - \mu_{\downarrow})) dE. \end{aligned} \quad (\text{A5})$$

(A6)

We notice the following relations:

$$\begin{aligned} \mu_{\uparrow, \downarrow} &= \mu \pm \mu_s, \\ \therefore f(E - \mu_{\uparrow, \downarrow}) &= f(E - (\mu \pm \mu_s)), \\ &= f(E - \mu) \pm \frac{\partial f}{\partial \mu} \mu_s, \\ \therefore f(E - \mu_{\uparrow}) - f(E - \mu_{\downarrow}) &= 2 \frac{\partial f}{\partial \mu} \mu_s. \end{aligned}$$

Since $\partial f / \partial \mu$ for a degenerate gas is approximately $\delta(E - \mu)$ ⁴⁰, we obtain on substitution of the above equation in Eq. (A5).

$$\begin{aligned} s &= \int g(E) \delta(E - \mu) \mu_s dE, \\ &= g(\mu) \mu_s. \end{aligned} \quad (\text{A7})$$

Hence we have a relation between spin density and spin chemical potential via density of states at the chemical potential. It might however be desirable to express the the above relation in terms of commonly used parameters such as conductivity (σ) and diffusion constant (D). This is achieved by comparing the diffusion current formulations used in Refs. 38 and 40.

The one dimensional particle diffusion current density in the formulation used in Ref. 40 is given by:

$$J_n = -D \frac{\partial n}{\partial x},$$

where D is the diffusion constant of the material, and subscript n reminds us that we are talking about a particle current. Correspondingly we can write net spin ‘‘particle’’ current:

$$\begin{aligned} J_{n\uparrow} - J_{n\downarrow} &= -D \frac{\partial(n\uparrow - n\downarrow)}{\partial x}, \\ &= -Dg(\mu) \frac{\partial\mu_s}{\partial x}, \end{aligned} \quad (\text{A8})$$

where we used Eq. (A7) in the last step above. Using formulation used in Ref. 38, we have

$$J_s = -\frac{\sigma}{2e} \frac{\partial\mu_s}{\partial x}.$$

Please note that the current density above has been expressed in units of charge current density for convenience³⁸. In order to compare the above expression to Eq. (A8), we need to divide the above equation by elementary charge (e) throughout. On comparison of the two particle current, we obtain the following relation:

$$g(\mu) = \frac{\sigma}{2e^2 D}.$$

Hence using the above equation in conjunction with Eq. (A7), we obtain the desired relation between spin imbalance density and spin accumulation:

$$s = \frac{\sigma}{2e^2 D} \mu_s.$$

Thus, for the $y(z)$ -polarized electrons, we get

$$n_{sy} = \frac{\sigma_N}{2e^2 D} \mu_{sy} \quad \text{and} \quad n_{sz} = \frac{\sigma_N}{2e^2 D} \mu_{sz}$$

Appendix B: Magnetic field of spin accumulation

The magnetic flux density (in the following referred to as *magnetic field*) originating from a magnetic moment \mathbf{m} is given by⁵²

$$\mathbf{B} = \frac{\mu_0}{4\pi r'^3} [3(\mathbf{m} \cdot \hat{\mathbf{r}}')\hat{\mathbf{r}}' - \mathbf{m}],$$

where \mathbf{r}' is the position vector from the magnetic moment to the point at which the flux density is calculated.

To obtain the magnetic stray field arising from the spin accumulation in the conducting strip, we integrate the contribution of the magnetic moments within the volume of the strip. With $n_s(\mathbf{r})$ being the spin accumulation density at point $\mathbf{r} = (x, y, z)$ with spin polarization $\hat{\mathbf{n}}$, the orientation-dependent magnetic moment density is $\gamma\hbar/2 \hat{\mathbf{n}}n_s(\mathbf{r})$, where γ denotes the gyromagnetic ratio of the material, respectively. Note that we treat the magnetic fields generated by the magnetic moments oriented along $\hat{\mathbf{z}}$ and $\hat{\mathbf{y}}$ initially independently and then calculate the vector sum of the magnetic fields.

We obtain for the magnetic field at $\mathbf{r}_p = (x_p, y_p, z_p)$, caused by the magnetization $\gamma\hbar/2\hat{\mathbf{n}}n_s(\mathbf{r})$ present in an infinitesimal volume element $dx dy dz$ around \mathbf{r}

$$d\mathbf{B} = \frac{\mu_0}{8\pi |\mathbf{r}_p - \mathbf{r}|^3} \left[3 \frac{\gamma\hbar\hat{\mathbf{n}}n_s(\mathbf{r}) \cdot (\mathbf{r}_p - \mathbf{r})}{|\mathbf{r}_p - \mathbf{r}|^2} (\mathbf{r}_p - \mathbf{r}) - \gamma\hbar\hat{\mathbf{n}}n_s(\mathbf{r}) \right] dx dy dz. \quad (\text{B1})$$

Employing Eqs. (4) and (B1), we calculate the magnetic field distribution outside the conductor originating from the spin accumulation. Due to the translational symmetry of the problem with respect to the $\hat{\mathbf{x}}$ -axis, the magnetic field does not depend on x_p which we choose to be 0.

We begin with the integration along the $\hat{\mathbf{x}}$ and $\hat{\mathbf{y}}$ -direction considering only the accumulation of $\hat{\mathbf{y}}$ -polarized spins, i. e. the contribution from n_{sy} . This magnetic field contribution is called $\mathbf{B}^{\hat{\mathbf{n}}\parallel\hat{\mathbf{y}}}$ in the following. Note that the integration can be done easily as n_{sy} does not depend on x and y . We obtain

$$\int_{x=-\infty}^{\infty} \int_{y=-y_0/2}^{y_0/2} d\mathbf{B}^{\hat{\mathbf{n}}\parallel\hat{\mathbf{y}}}(\mathbf{r}, \mathbf{r}_p) = \frac{\mu_0\gamma\hbar n_{sy}(z)}{8\pi} \left[\left(\begin{array}{c} 0 \\ \frac{2(y_p - \frac{y_0}{2})}{(y_p - \frac{y_0}{2})^2 + (z_p - z)^2} \\ \frac{2(z_p - z)}{(y_p - \frac{y_0}{2})^2 + (z_p - z)^2} \end{array} \right) - \left(\begin{array}{c} 0 \\ \frac{2(y_p + \frac{y_0}{2})}{(y_p + \frac{y_0}{2})^2 + (z_p - z)^2} \\ \frac{2(z_p - z)}{(y_p + \frac{y_0}{2})^2 + (z_p - z)^2} \end{array} \right) \right] dz. \quad (\text{B2})$$

An analogous integration along the $\hat{\mathbf{x}}$ and $\hat{\mathbf{z}}$ -direction for the magnetic field contribution from n_{sz} yields

$$\int_{x=-\infty}^{\infty} \int_{z=-z_0/2}^{z_0/2} d\mathbf{B}^{\hat{\mathbf{n}}\parallel\hat{\mathbf{z}}}(\mathbf{r}, \mathbf{r}_p) = \frac{\mu_0\gamma\hbar n_{sz}(y)}{8\pi} \left[\left(\begin{array}{c} 0 \\ \frac{2(y_p - y)}{(y_p - y)^2 + (z_p - \frac{z_0}{2})^2} \\ \frac{2(z_p - \frac{z_0}{2})}{(y_p - y)^2 + (z_p - \frac{z_0}{2})^2} \end{array} \right) - \left(\begin{array}{c} 0 \\ \frac{2(y_p - y)}{(y_p - y)^2 + (z_p + \frac{z_0}{2})^2} \\ \frac{2(z_p + \frac{z_0}{2})}{(y_p - y)^2 + (z_p + \frac{z_0}{2})^2} \end{array} \right) \right] dy. \quad (\text{B3})$$

For a full quantitative modelling of the magnetic field dis-

tribution in the surrounding of the conductor, we perform

the remaining integration over the y - and z -dimensions of Eqs. (B2) and (B3) numerically. To this end, we use the spatially dependent spin accumulation density from Eqs. (4) – (6).

Before discussing the numerical results below, we turn to a simplified picture where we consider all spins to be located at the conductor's surface (as indicated in Fig. 1)—a situation which can be treated analytically. This approximation agrees well with the exact solution when the point of interest is located much further away from the conductor as compared to the spin relaxation length (~ 1 nm for platinum). In this case, we approximate the spin accumulation density for the $\hat{\mathbf{y}}$ -polarized electrons as

$$n_{sy}(z) \approx \tilde{n}_{sy} \left[\delta \left(z - \frac{z_0}{2} \right) - \delta \left(z + \frac{z_0}{2} \right) \right] \quad (\text{B4})$$

with $\delta(x)$ the Dirac delta distribution and $\tilde{n}_{sy} := \int_0^{z_0/2} n_{sy}(z) dz$. Combining Eqs. (4) and (6), we get

$$\tilde{n}_{sy} = -\frac{j_e \theta \lambda^2}{De} \left(1 - \frac{1}{\cosh \left(\frac{z_0}{2\lambda} \right)} \right) \quad (\text{B5})$$

Performing the integration for the z -direction in Eq. (B2) we obtain for the magnetic stray field caused by the spin accumulation \tilde{n}_{sy}

$$\mathbf{B}^{\hat{\mathbf{n}}\|\hat{\mathbf{y}}}(\mathbf{r}_p) = \frac{\mu_0 \gamma \hbar \tilde{n}_{sy}}{8\pi} \mathbf{F}(y_0, z_0; \mathbf{r}_p)$$

with

$$\mathbf{F}(y_0, z_0; \mathbf{r}_p) = \left[\left(\begin{array}{c} 0 \\ \frac{2(y_p - y_0/2)}{(y_p - y_0/2)^2 + (z_p - z_0/2)^2} \\ \frac{2(z_p - z_0/2)}{(y_p - y_0/2)^2 + (z_p - z_0/2)^2} \end{array} \right) - \left(\begin{array}{c} 0 \\ \frac{2(y_p + y_0/2)}{(y_p + y_0/2)^2 + (z_p - z_0/2)^2} \\ \frac{2(z_p - z_0/2)}{(y_p + y_0/2)^2 + (z_p - z_0/2)^2} \end{array} \right) - \left(\begin{array}{c} 0 \\ \frac{2(y_p - y_0/2)}{(y_p - y_0/2)^2 + (z_p + z_0/2)^2} \\ \frac{2(z_p + z_0/2)}{(y_p - y_0/2)^2 + (z_p + z_0/2)^2} \end{array} \right) + \left(\begin{array}{c} 0 \\ \frac{2(y_p + y_0/2)}{(y_p + y_0/2)^2 + (z_p + z_0/2)^2} \\ \frac{2(z_p + z_0/2)}{(y_p + y_0/2)^2 + (z_p + z_0/2)^2} \end{array} \right) \right] \quad (\text{B6})$$

For the magnetic field contribution of the z -polarized electrons, we find correspondingly

$$\mathbf{B}^{\hat{\mathbf{n}}\|\hat{\mathbf{z}}}(\mathbf{r}_p) = -\frac{\mu_0 \gamma \hbar \tilde{n}_{sz}}{8\pi} \mathbf{F}(y_0, z_0; \mathbf{r}_p)$$

with

$$\tilde{n}_{sz} = \frac{j_e \theta \lambda^2}{De} \left(1 - \frac{1}{\cosh \left(\frac{y_0}{2\lambda} \right)} \right). \quad (\text{B7})$$

In total, the magnetic field at point \mathbf{r}_p arising from the spin polarization in the conducting strip is given by

$$\begin{aligned} \mathbf{B}(\mathbf{r}_p) &= \mathbf{B}^{\hat{\mathbf{n}}\|\hat{\mathbf{y}}}(\mathbf{r}_p) + \mathbf{B}^{\hat{\mathbf{n}}\|\hat{\mathbf{z}}}(\mathbf{r}_p) \\ &= \frac{\mu_0 \gamma \hbar j_e \theta \tau}{8\pi e} \left(\frac{1}{\cosh \left(\frac{y_0}{2\lambda} \right)} - \frac{1}{\cosh \left(\frac{z_0}{2\lambda} \right)} \right) \mathbf{F}(y_0, z_0; \mathbf{r}_p) \end{aligned} \quad (\text{B8})$$

Obviously, the magnetic stray field is proportional to the spin Hall angle, the spin-flip time and the applied current density through the conductor. Regarding the geometry, a square cross-section of the conductor (i. e. $y_0 = z_0$) would imply a vanishing stray field as Eq. B8 shows. This is a consequence of the symmetry of the problem and holds for the analytical approximation as well as for the full numerical calculation. As we are interested in maximizing the stray field around the conductor, we suggest

a very thin ($y_0 \lesssim 3$ nm) metal strip with $z_0 \gg y_0$ for the experimental investigation of the calculated stray field.

Appendix C: Oersted field

The magnetic field induced by an infinitesimal conductor cross-section $dy dz$ around \mathbf{r} can be written as⁵³

$$d\mathbf{B}_{\text{Oer}} = \frac{\mu_0}{2\pi |\mathbf{r}_p - \mathbf{r}|^2} \mathbf{j} \times (\mathbf{r}_p - \mathbf{r}) dy dz. \quad (\text{C1})$$

The total Oersted field arising from the (uniform) current density $\mathbf{j} = j_e \hat{\mathbf{x}}$ in the conducting strip can thus be calculated by integrating $d\mathbf{B}_{\text{Oer}}$ over the cross-section of the strip. The integral can be solved analytically but the resulting expression is unwieldy and therefore not given here. Figure 4 shows the spatial distribution of the Oersted field around the conductor. It has its maximum of about 16 μT at the left and right edge of the strip. For $r_p \gg y_0, z_0$, the Oersted field decays proportional to $1/r_p$ as expected for the farfield of a current in a wire. Thus, in the farfield, the Oersted field dominates the stray field. This is also illustrated in Fig. 5, where the ratio $|\mathbf{B}|/|\mathbf{B}_{\text{Oer}}|$ is plotted as a function of the sensor position \mathbf{r}_p . Only for small distance from the conducting strip, the stray field exceeds the Oersted field.

Nevertheless, the spatial dependence of the Oersted field significantly differs from that of the magnetic stray field of spin accumulation. Thus, using a spatially resolved magnetic field sensing technique would in principle allow to differentiate between stray field and Oersted field.

- * huebl@wmi.badw.de
- ¹ Igor Zutic, Jaroslav Fabian, and S. Das Sarma, “Spintronics: Fundamentals and applications,” *Reviews of Modern Physics* **76**, 323–410 (2004).
 - ² S. A. Wolf, D. D. Awschalom, R. A. Buhrman, J. M. Daughton, S. von Molnár, M. L. Roukes, A. Y. Chtchelkanova, and D. M. Treger, “Spintronics: A spin-based electronics vision for the future,” *Science* **294**, 1488 (2001).
 - ³ J.C. Slonczewski, “Current-driven excitation of magnetic multilayers,” *Journal of Magnetism and Magnetic Materials* **159**, L1 – L7 (1996).
 - ⁴ L. Berger, “Emission of spin waves by a magnetic multilayer traversed by a current,” *Phys. Rev. B* **54**, 9353–9358 (1996).
 - ⁵ D.C. Ralph and M.D. Stiles, “Spin transfer torques,” *Journal of Magnetism and Magnetic Materials* **320**, 1190 – 1216 (2008).
 - ⁶ Stuart S. P. Parkin, Masamitsu Hayashi, and Luc Thomas, “Magnetic domain-wall race-track memory,” *Science* **320**, 190–194 (2008), <http://science.sciencemag.org/content/320/5873/190.full.pdf>.
 - ⁷ Johan Åkerman, “Toward a universal memory,” *Science* **308**, 508–510 (2005), <http://science.sciencemag.org/content/308/5721/508.full.pdf>.
 - ⁸ M. I. Dyakonov and A. V. Khaetskii, “Spin hall effect,” in *Spin Physics in Semiconductors*, edited by Michel I. Dyakonov (Springer Berlin Heidelberg, Berlin, Heidelberg, 2008) pp. 211–243.
 - ⁹ J. E. Hirsch, “Spin hall effect,” *Physical Review Letters* **83**, 1834–1837 (1999).
 - ¹⁰ E. Saitoh, M. Ueda, H. Miyajima, and G. Tatara, “Conversion of spin current into charge current at room temperature: Inverse spin-hall effect,” *Applied Physics Letters* **88**, 182509 (2006), <http://dx.doi.org/10.1063/1.2199473>.
 - ¹¹ Jairo Sinova, Sergio O. Valenzuela, J. Wunderlich, C. H. Back, and T. Jungwirth, “Spin hall effects,” *Rev. Mod. Phys.* **87**, 1213–1260 (2015).
 - ¹² Saburo Takahashi and Sadamichi Maekawa, “Spin current, spin accumulation and spin hall effect,” *Science and Technology of Advanced Materials* **9**, 014105 (2008).
 - ¹³ Non-magnetic here shall denote metals that do not show long-range magnetic order such as ferro- or ferrimagnetism.
 - ¹⁴ Mathias Weiler, Matthias Althammer, Michael Schreier, Johannes Lotze, Matthias Pernpeintner, Sibylle Meyer, Hans Huebl, Rudolf Gross, Akashdeep Kamra, Jiang Xiao, *et al.*, “Experimental test of the spin mixing interface conductivity concept,” *Physical review letters* **111**, 176601 (2013).
 - ¹⁵ Yaroslav Tserkovnyak, Arne Brataas, and Gerrit E. W. Bauer, “Spin pumping and magnetization dynamics in metallic multilayers,” *Physical Review B* **66**, 224403 (2002).
 - ¹⁶ F. D. Czeschka, L. Dreher, M. S. Brandt, M. Weiler, M. Althammer, I.-M. Imort, G. Reiss, A. Thomas, W. Schoch, W. Limmer, H. Huebl, R. Gross, and S. T. B. Goennenwein, “Scaling behavior of the spin pumping effect in ferromagnet-platinum bilayers,” *Physical Review Letters* **107**, 046601 (2011).
 - ¹⁷ Mark Johnson and R. H. Silsbee, “Interfacial charge-spin coupling: Injection and detection of spin magnetization in metals,” *Physical Review Letters* **55**, 1790–1793 (1985).
 - ¹⁸ K. Uchida, S. Takahashi, K. Harii, J. Ieda, W. Koshibae, K. Ando, S. Maekawa, and E. Saitoh, “Observation of the spin seebeck effect,” *Nature* **455**, 778–781 (2008).
 - ¹⁹ C. M. Jaworski, J. Yang, S. Mack, D. D. Awschalom, J. P. Heremans, and R. C. Myers, “Observation of the spin-seebeck effect in a ferromagnetic semiconductor,” *Nature Materials* **9**, 898–903 (2010).
 - ²⁰ Jiang Xiao, Gerrit E. W. Bauer, Ken-chi Uchida, Eiji Saitoh, and Sadamichi Maekawa, “Theory of magnon-driven spin seebeck effect,” *Physical Review B* **81**, 214418 (2010).
 - ²¹ H. Nakayama, M. Althammer, Y.-T. Chen, K. Uchida, Y. Kajiwara, D. Kikuchi, T. Ohtani, S. Geprägs, M. Opel, S. Takahashi, R. Gross, G. E. W. Bauer, S. T. B. Goennenwein, and E. Saitoh, “Spin hall magnetoresistance induced by a nonequilibrium proximity effect,” *Phys. Rev. Lett.* **110**, 206601 (2013).
 - ²² Matthias Althammer, Sibylle Meyer, Hiroyasu Nakayama, Michael Schreier, Stephan Altmannshofer, Mathias Weiler, Hans Huebl, Stephan Geprägs, Matthias Opel, Rudolf Gross, Daniel Meier, Christoph Klewe, Timo Kuschel, Jan-Michael Schmalhorst, Günter Reiss, Liming Shen, Arunava Gupta, Yan-Ting Chen, Gerrit E. W. Bauer, Eiji Saitoh, and Sebastian T. B. Goennenwein, “Quantitative study of the spin hall magnetoresistance in ferromagnetic insulator/normal metal hybrids,” *Phys. Rev. B* **87**, 224401 (2013).
 - ²³ Yan-Ting Chen, Saburo Takahashi, Hiroyasu Nakayama, Matthias Althammer, Sebastian T. B. Goennenwein, Eiji Saitoh, and Gerrit E. W. Bauer, “Theory of spin hall magnetoresistance,” *Phys. Rev. B* **87**, 144411 (2013).
 - ²⁴ Yan-Ting Chen, Saburo Takahashi, Hiroyasu Nakayama, Matthias Althammer, Sebastian T B Goennenwein, Eiji Saitoh, and Gerrit E W Bauer, “Theory of spin hall magnetoresistance (smr) and related phenomena,” *Journal of Physics: Condensed Matter* **28**, 103004 (2016).
 - ²⁵ Y. K. Kato, R. C. Myers, A. C. Gossard, and D. D. Awschalom, “Observation of the spin hall effect in semiconductors,” *Science* **306**, 1910 (2004).
 - ²⁶ N. P. Stern, S. Ghosh, G. Xiang, M. Zhu, N. Samarth, and D. D. Awschalom, “Current-induced polarization and the spin hall effect at room temperature,” *Physical Review Letters* **97**, 126603 (2006).
 - ²⁷ C. Stamm, C. Murer, M. Berritta, J. Feng, M. Gabureac, P. M. Oppeneer, and P. Gambardella, “Magneto-optical detection of the spin hall effect in pt and w thin films,” *Phys. Rev. Lett.* **119**, 087203 (2017).
 - ²⁸ Sibylle Meyer, Matthias Althammer, Stephan Geprägs, Matthias Opel, Rudolf Gross, and Sebastian T. B. Goennenwein, “Temperature dependent spin transport properties of platinum inferred from spin hall magnetoresistance measurements,” *Applied Physics Letters* **104**, 242411 (2014), <http://dx.doi.org/10.1063/1.4885086>.
 - ²⁹ N. Vlietstra, J. Shan, V. Castel, B. J. van Wees, and J. Ben Youssef, “Spin-hall magnetoresistance in platinum on yttrium iron garnet: Dependence on platinum thickness and in-plane/out-of-plane magnetization,” *Phys. Rev. B* **87**, 184421 (2013).
 - ³⁰ J R Maze, P L Stanwix, J S Hodges, S Hong, J M Taylor, P Cappellaro, L Jiang, M V Gurudev Dutt, E Togan, A S Zibrov, A Yacoby, R L Walsworth, and M D Lukin,

- “Nanoscale magnetic sensing with an individual electronic spin in diamond,” *Nature* **455**, 644–647 (2008).
- ³¹ M S Grinolds, S Hong, P Maletinsky, L Luan, M D Lukin, R L Walsworth, and A Yacoby, “Nanoscale magnetic imaging of a single electron spin under ambient conditions,” *Nature Physics* **9**, 215–219 (2013).
- ³² P Maletinsky, S Hong, M S Grinolds, B Hausmann, M D Lukin, R L Walsworth, M Loncar, and A Yacoby, “A robust scanning diamond sensor for nanoscale imaging with single nitrogen-vacancy centres,” *Nature Nanotechnology* **7**, 320–324 (2012).
- ³³ D. Rugar, R. Budakian, H. J. Mamin, and B. W. Chui, “Single spin detection by magnetic resonance force microscopy,” *Nature* **430**, 329–332 (2004).
- ³⁴ J M Taylor, P Cappellaro, L Childress, L Jiang, D Budker, P R Hemmer, A Yacoby, R Walsworth, and M D Lukin, “High-sensitivity diamond magnetometer with nanoscale resolution,” *Nature Physics* **4**, 810–816 (2008).
- ³⁵ Denis Vasyukov, Yonathan Anahory, Lior Embon, Dorri Halbertal, Jo Cuppens, Lior Neeman, Amit Finkler, Yehonathan Segev, Yuri Myasodov, Michael L Rappaport, Martin E Huber, and Eli Zeldov, “A scanning superconducting quantum interference device with single electron spin sensitivity,” *Nature Nanotechnology* **8**, 639–644 (2013).
- ³⁶ John R Kirtley, Lisa Paulius, Aaron J Rosenberg, Johanna C Palmstrom, Connor M Holland, Eric M Spanton, Daniel Schiessl, Colin L Jermain, Jonathan Gibbons, Y K K Fung, Martin E Huber, Daniel C Ralph, Mark B Ketchen, Gerald W Gibson Jr, and Kathryn A Moler, “Scanning SQUID susceptometers with sub-micron spatial resolution,” *Review Of Scientific Instruments* **87**, 093702 (2016).
- ³⁷ H. Luetkens, J. Korecki, E. Morenzoni, T. Prokscha, M. Birke, H. Glückler, R. Khasanov, H.-H. Klauss, T. Ślezak, A. Suter, E. M. Forgan, Ch. Niedermayer, and F. J. Litterst, “Observation of the conduction electron spin polarization in the ag spacer of a Fe/Ag/Fe trilayer,” *Phys. Rev. Lett.* **91**, 017204 (2003).
- ³⁸ Yan-Ting Chen, Saburo Takahashi, Hiroyasu Nakayama, Matthias Althammer, Sebastian T. B. Goennenwein, Eiji Saitoh, and Gerrit E. W. Bauer, “Theory of spin hall magnetoresistance,” *Physical Review B* **87**, 144411 (2013).
- ³⁹ A. Aqeel, I. J. Vera-Marun, Z. Salman, T. Prokscha, A. Suter, B. J. van Wees, and T. T. M. Palstra, “Probing current-induced magnetic fields in au—yig heterostructures with low-energy muon spin spectroscopy,” *Applied Physics Letters* **110**, 062409 (2017), <http://dx.doi.org/10.1063/1.4975487>.
- ⁴⁰ Jaroslav Fabian, Alex Matos-Abiague, Christian Ertler, Peter Stano, and Igor uti, “Semiconductor spintronics,” *Acta Physica Slovaca. Reviews and Tutorials* **57**, 565–907 (2007).
- ⁴¹ O. Mosendz, V. Vlaminck, J. E. Pearson, F. Y. Fradin, G. E. W. Bauer, S. D. Bader, and A. Hoffmann, “Detection and quantification of inverse spin hall effect from spin pumping in permalloy/normal metal bilayers,” *Phys. Rev. B* **82**, 214403 (2010).
- ⁴² Mark Johnson and Jefferson Byers, “Charge and spin diffusion in mesoscopic metal wires and at ferromagnet/nonmagnet interfaces,” *Physical Review B* **67**, 125112 (2003).
- ⁴³ This value is calculated from Ref.¹¹, Table I and Ref.11 therein.
- ⁴⁴ Here, we have compared the calculated n_{si} to the experimentally determined free electron density in platinum thin films, $n = 1.6 \times 10^{28} \text{ m}^{-3}$ (see Ref. 54).
- ⁴⁵ z_0 can be chosen large compared to y_0 without significantly decreasing the stray field!
- ⁴⁶ Ernst Meyer, Hans Josef Hug, and Roland Bennewitz, *Scanning Probe Microscopy* (Springer, 2004).
- ⁴⁷ Alexander Schwarz and Roland Wiesendanger, “Magnetic sensitive force microscopy,” *Nano Today* **3**, 28–39 (2008).
- ⁴⁸ F.A. Ferri, M.A. Pereira-da Silva, and E. (Jr.) Marega, “Atomic force microscopy - imaging, measuring and manipulating surfaces at the atomic scale,” (InTech, 2012) Chap. Magnetic Force Microscopy: Basic Principles and Applications, pp. 39–56.
- ⁴⁹ D. Jiles, *Introduction to magnetism and magnetic materials* (Chapman and Hall, 1991).
- ⁵⁰ H. J. Mamin and D. Rugar, “Sub-attonewton force detection at millikelvin temperatures,” *Applied Physics Letters* **79**, 3358–3360 (2001).
- ⁵¹ Eric Straver, *Cantilever-based measurements on nanomagnets and superconductors*, Ph.D. thesis, Stanford University (2004).
- ⁵² John David Jackson, *Classical Electrodynamics* (Wiley, 1998).
- ⁵³ We assume the conductor to be aligned along the x -axis.
- ⁵⁴ Gerd Fischer, Horst Hoffmann, and Johann Vancea, “Mean free path and density of conductance electrons in platinum determined by the size effect in extremely thin films,” *Physical Review B* **22**, 6065–6073 (1980).